



**HAL**  
open science

## Robustness to spatially-correlated speckle in Plug-and-Play PolSAR despeckling

Cristiano Ulundu-Mendes, Loïc Denis, Charles-Alban Deledalle, Florence  
Tupin

► **To cite this version:**

Cristiano Ulundu-Mendes, Loïc Denis, Charles-Alban Deledalle, Florence Tupin. Robustness to spatially-correlated speckle in Plug-and-Play PolSAR despeckling. 2023. hal-04159195v1

**HAL Id: hal-04159195**

**<https://telecom-paris.hal.science/hal-04159195v1>**

Preprint submitted on 11 Jul 2023 (v1), last revised 30 Aug 2024 (v2)

**HAL** is a multi-disciplinary open access archive for the deposit and dissemination of scientific research documents, whether they are published or not. The documents may come from teaching and research institutions in France or abroad, or from public or private research centers.

L'archive ouverte pluridisciplinaire **HAL**, est destinée au dépôt et à la diffusion de documents scientifiques de niveau recherche, publiés ou non, émanant des établissements d'enseignement et de recherche français ou étrangers, des laboratoires publics ou privés.

# Robustness to spatially-correlated speckle in Plug-and-Play PolSAR despeckling

Cristiano Ulondu Mendes, Loïc Denis, Charles Deledalle, Florence Tupin

**Abstract**—Synthetic Aperture Radar (SAR) provides valuable information about the Earth’s surface in all-weather and day-and-night conditions. Due to the inherent presence of speckle phenomenon, a filtering step is often required to improve the performance of downstream tasks. In this paper, we focus on dealing with the spatial correlations of speckle, which impacts negatively many of the existing speckle filters. Taking advantage of the flexibility of variational methods based on the Plug-and-Play strategy, we propose to use a Gaussian denoiser trained to restore SAR scenes corrupted by colored Gaussian noise with correlation structures typical of a range of radar sensors. Our approach improves the robustness of Plug-and-Play despeckling techniques. Experiments conducted on simulated and real polarimetric SAR images show that the proposed method removes speckle efficiently in the presence of spatial correlations without introducing artifacts, with a good level of detail preservation. Our method can be readily applied, without network re-training or fine-tuning, to filter SAR images from various sensors, acquisition modes (SAR, PolSAR, InSAR, PolInSAR), spatial resolution, and even benefit from co-registered multi-temporal stacks, when available. The code of the trained models is made freely available at <https://gitlab.telecom-paris.fr/ring/mulog-drunet>.

**Index Terms**—SAR, polarimetry, image despeckling, deep learning, correlated speckle.

## I. INTRODUCTION

**P**OLARIMETRIC synthetic aperture radar (SAR) images offer rich information of the back-scattering mechanisms occurring throughout the scene [1]. They are particularly useful to retrieve physical information for land, ice, ocean, forest, or urban applications [2]. Yet, due to the speckle phenomenon, these images, like all SAR images, are difficult to analyze. The speckle phenomenon occurs due to the coherent summation of many elementary echoes within a radar resolution cell. It appears in the images in the form of strong signal-dependent fluctuations. The development of efficient speckle filtering methods that preserve at best the content of the images is therefore crucial for many applications, in particular those requiring the full spatial resolution provided by the instrument. Many approaches have been proposed in the past three decades to address this problem. They can be divided into several groups:

C. Ulondu Mendes and F. Tupin are with LTCI, Télécom Paris, Institut Polytechnique de Paris, Palaiseau, France, e-mail: [forename.name@telecom-paris.fr](mailto:forename.name@telecom-paris.fr).

L. Denis is with Université Jean Monnet Saint-Etienne, CNRS, Institut d’Optique Graduate School, Laboratoire Hubert Curien UMR 5516, F-42023, SAINT-ETIENNE, France, and also with LTCI, Télécom Paris, Institut Polytechnique de Paris, Palaiseau, France, e-mail: [loic.denis@univ-st-etienne.fr](mailto:loic.denis@univ-st-etienne.fr).

C. Deledalle is with Brain Corporation, 10182 Telesis Ct, San Diego, CA 92121, USA.

**Local filtering:** These methods aim to attenuate the fluctuations at each pixel by combining the information within a small neighbourhood. Examples are the Lee filters [3], the Kuan filters [4], or the simplest one, the boxcar filter, which consists in a simple moving average.

**Patch-based techniques:** The target pixel is still denoised by combining the values of pixels contained within a neighborhood (this time, a much larger neighborhood defined by the so-called search window is used). The importance of each pixel of the search window is derived based on patch similarity. By discarding dissimilar pixels, patch-based methods perform adaptive smoothing: speckle is strongly reduced in homogeneous areas while geometrical and textural structures are preserved [5].

**Variational methods:** They formulate the restoration problem as the minimization of a cost function involving a data fidelity term that accounts for the statistics of speckle and a regularization term that promotes noise-free images (for example: smooth images with sharp edges [6]–[9]).

**Deep learning:** Neural networks with a large number of parameters are trained in order to learn how speckle fluctuations can be separated from the content of SAR scenes [10], [11]. In the case of single-channel SAR images, many training strategies have been proposed [12]: (i) supervised learning [13], [14] where pairs of speckle-free and corrupted images are provided (first, despeckled images are produced by averaging a long time series of co-registered images, or by degrading the resolution of a very high resolution image, then, corrupted versions of these images are generated with synthetic speckle); (ii) semi-supervised learning uses pairs of images of the same area to train the network to predict the second image with only the first image as input (if speckle is temporally decorrelated, only the underlying reflectivity is output by the network provided that adequate change compensation is performed [15]); (iii) self-supervised learning masks partially the input image: the central pixel in blind-spot approaches [16] or either the real or the imaginary component in MERLIN [17]. Despeckling polarimetric SAR images with deep learning is much more challenging than the case of single-channel intensity images: polarimetric information is represented in the form of complex-valued covariance matrices. The networks have to adapt both to the statistics of speckle (involving scene-dependent correlations between polarimetric channels) and to the high variability of polarimetric SAR scenes. Several approaches have been considered to address these difficulties. Foucher *et al.* [18] follow an additive

decomposition of polarimetric SAR covariance matrices into the speckle-free covariances and two additional signal-dependent corruption terms. They then derive an iterative despeckling scheme involving a shallow neural network to suppress these additive corruptions. Most other approaches use a matrix logarithm transform to turn the speckle into an almost signal-independent additive component. This component is then suppressed thanks to an iterative processing [19] or in a single-step with a network involving only real-valued operations [20], or complex-valued processing [21]. Another direction consists of using a neural network to compute the relative weights of pixels in the final estimation. This can be seen as an extension of pixel-selection methods introduced by the seminal works of Lee [22], [23] and later particularly developed by patch-based approaches. First introduced to despeckle intensity images [24], this idea has been recently extended to polarimetric SAR images [25].

The Plug-and-Play framework (PnP) [26], [27] can be seen as a bridge between variational methods and the other classes, as it allows Gaussian denoisers of any form to be included within an iterative minimization algorithm derived from the statistical model of speckle.

Many of the proposed speckle removal methods perform poorly when applied to real SAR images because they assume that the speckle is spatially independent, while in practice it is spatially correlated. Preprocessing steps that decorrelate the speckle either modify the appearance of the SAR scene (side-lobes of the bright targets) or degrades the spatial resolution (by subsampling) [28]. Rather than whitening speckle [29], [30], it is preferable to design restoration methods that are robust to the spatial correlations of speckle to preserve the spectral apodization and sampling of the original SAR images. Only few despeckling methods are robust to speckle correlations. In single-channel despeckling, training a neural network to process images with spatially correlated speckle provides robustness to these correlations. For multi-channel SAR images such as in PolSAR, robustness to spatially correlated speckle has not been addressed yet by deep-learning-based methods. To the best of our knowledge, the only type of methods that can be applied to PolSAR images without a preprocessing step to reduce speckle correlations is the non-local methods [31]. The goal of this paper is to propose a despeckling framework for monochannel and multichannel SAR images that is robust to spatial correlation through the joint exploitation of statistical models and deep neural networks. Our main contributions are summarized as follows:

- 1) we provide a despeckling framework robust to the spatial correlations of speckle observed for a range of sensors, without requiring a decorrelating preprocessing step;
- 2) we enable to handle single-channel (intensity) or multi-channel (polarimetric and/or interferometric) SAR images from various sensors with a single neural network (no re-training necessary);
- 3) when a temporal stack of images is available, we enable to perform a multi-temporal polarimetric filtering based on the ratio with a virtually speckle-free "super-image"

(extension of our preliminary work on multi-temporal polarimetric filtering presented at IGARSS [32]);

- 4) We make the source code available for reproducible research.

## II. IMPROVEMENT OF MULOG'S ROBUSTNESS TO SPATIALLY CORRELATED SPECKLE

Our method builds on the generic despeckling method MuLoG [27], [33]. In the following paragraphs, we first recall the statistical model of speckle and the main steps of MuLoG, then we describe how we modified the Gaussian denoiser at the core of MuLoG in order to improve the robustness to spatial correlations.

### A. Statistical model of multi-channel SAR images

An important step in the development of a variational filtering method is the selection of an adequate statistical model. A widely used model to describe speckle in SAR images is the Goodman model [34] in which the diffusion vector  $\mathbf{k} \in \mathbb{C}^d$  at a given pixel of a  $d$ -channel SAR image follows a  $d$ -variate complex circular Gaussian distribution  $\mathcal{N}_c(\Sigma)$  defined by the probability density function (PDF):

$$p(\mathbf{k}|\Sigma) = \frac{1}{\pi^d |\Sigma|} \exp(-\mathbf{k}^* \Sigma^{-1} \mathbf{k}) \quad (1)$$

where  $*$  refers to the Hermitian transpose and  $|\Sigma|$  denotes the determinant of matrix  $\Sigma$ . This PDF is fully characterized by the covariance matrix  $\Sigma = \mathbb{E}[\mathbf{k}\mathbf{k}^*] \in \mathbb{C}^{d \times d}$ , a Hermitian positive definite matrix that contains all the polarimetric and/or interferometric information of interest. It is common practice to pre-estimate  $\Sigma$  by computing the empirical covariance  $\mathbf{C}$  over a relatively small neighborhood  $\omega$  (e.g., a square window centered on the pixel of interest). In the absence of spatial correlations of speckle, the number of pixels  $L$  in  $\omega$  defines the number of looks (the number of independent looks is strictly smaller in the case of correlations). The empirical covariance  $\mathbf{C}$  follows a Wishart distribution [35] parameterized by  $\Sigma$  and  $L$ :  $\mathbf{C} \sim \mathcal{W}(\Sigma; L)$ , and its PDF is well-defined when  $L \geq d$ :

$$p_{\mathbf{C}}(\mathbf{C}|\Sigma) = \frac{L^d |\mathbf{C}|^{L-d}}{\Gamma_d(L) |\Sigma|^L} \exp(-L \text{tr}(\Sigma^{-1} \mathbf{C})) \quad (2)$$

where  $\Gamma_d(L) = \pi^{d(d-1)/2} \prod_{l=1}^d \Gamma(L-l+1)$  and  $\Gamma$  is the gamma function.

In this paper, we focus on polarimetric SAR imagery (PolSAR), i.e. the case where  $d = 3$ , yet our method can readily be applied to interferometric (InSAR or PolInSAR) images.

Although widely used, the Goodman model of eq. (1) does not account for the transfer function of the SAR system. Most radar image providers apply spectral apodization and oversampling to reduce the sidelobes of strong scatterers and adjust the pixel size (see figure 1), resulting in images corrupted by spatially correlated speckle noise. Spatial correlation of the speckle leads to severe artifacts with most despeckling algorithms unless a proper preprocessing step is applied [28].

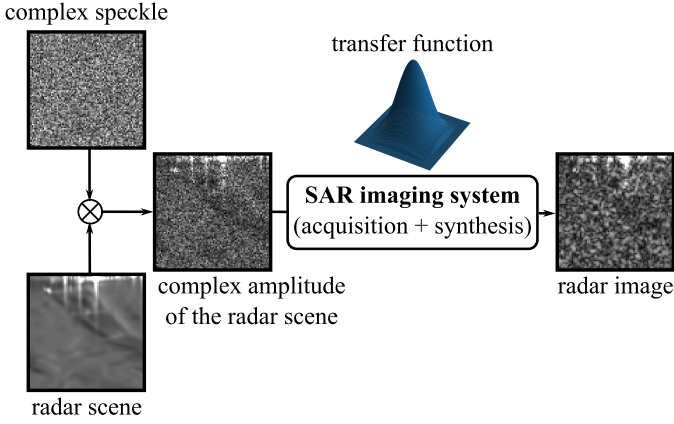


Figure 1: Generative model of SAR images.

### B. Brief recall of the MuLoG framework

The MuLoG framework corresponds to the extension to the multi-channel case of the variational approach MIDAL (Multiplicative Image Denoising by Augmented Lagrangian) [7] and the application of the Plug-and-Play (PnP) approach. MIDAL was introduced to estimate, in the logarithmic domain, the underlying reflectivity of a scene from the  $L$ -look intensity image. The authors of [7] highlight three benefits of this domain change. Firstly, taking the logarithm of the intensity transforms the multiplicative nature of the speckle into an additive fluctuation with constant variance; secondly, it facilitates the resolution of the optimization problem derived from the MAP formulation by removing the positivity constraint under the multiplicative model; and finally, it makes the data fidelity term convex. MuLoG builds on these advantages to denoise PolSAR images which are much more challenging due to the complex relationships binding the different terms of the covariance matrices that must be preserved during the filtering process. Rather than defining an explicit regularization term, it adopts a PnP strategy: it includes a denoising step performed by an off-the-shelf denoiser suitable to remove additive white Gaussian noise in images. It can benefit readily from the continuing progress of research on Gaussian denoisers.

Let  $\mathbf{C}$  be the speckled version of an  $n$ -pixels image of covariance matrices  $\mathbf{\Sigma} \in \mathbb{C}^{n \times d \times d}$ , where  $d$  is the number of channels ( $d = 3$  in monostatic polarimetry). If the input data are available in the form of SLC diffusion vectors  $\mathbf{k}$ , full-rank covariance matrices  $\mathbf{C}$  with a controlled condition number can be formed by modifying the eigenvalues of the rank-one matrices  $\mathbf{k}\mathbf{k}^*$  (see Algorithm 5 and Sec. 4.2 in [33]), without altering the spatial resolution. The main steps to filter the image  $\mathbf{C}$  with the MuLoG filtering framework are the following [27], [33]:

- 1) at each pixel  $i$ , the matrix logarithm of the covariance matrix  $\mathbf{C}_i$  is computed, leading to an image  $\tilde{\mathbf{C}} \in \mathbb{C}^{n \times d \times d}$ .
- 2) the  $d^2$  real-valued degrees of freedom of these log-transformed covariance matrices are extracted and whitened, leading to  $\mathbf{y} \in \mathbb{R}^{n \times d^2}$ .
- 3) the maximum *a posteriori* estimator associated with the

filtering of  $\mathbf{y}$  is given by:

$$\hat{\mathbf{x}} \in \underset{\mathbf{x} \in \mathbb{R}^{n \times d^2}}{\operatorname{argmin}} - \log(p_{\mathbf{y}}(\mathbf{y}|\mathbf{x})) - \underbrace{\log(p_{\mathbf{x}}(\mathbf{x}))}_{\mathcal{R}(\mathbf{x})} \quad (3)$$

Solving this problem with the alternating directions method of multipliers (ADMM) consists of iterating the following steps:

$$\hat{\mathbf{z}}^i \leftarrow \underset{\mathbf{z}^i \in \mathbb{R}^n}{\operatorname{argmin}} \frac{\beta}{2} \|\mathbf{z}^i - \hat{\mathbf{x}}^i + \hat{\mathbf{m}}^i\|^2 + \mathcal{R}_i(\mathbf{z}^i)$$

for each real-valued channel  $i$  from 1 to  $d^2$ , (4)

$$\hat{\mathbf{m}} \leftarrow \hat{\mathbf{m}} + \hat{\mathbf{z}} - \hat{\mathbf{x}} \quad (5)$$

(Lagrange multipliers update)

$$\hat{\mathbf{x}} \leftarrow \underset{\mathbf{x} \in \mathbb{R}^{n \times d^2}}{\operatorname{argmin}} \frac{\beta}{2} \|\mathbf{x} - \hat{\mathbf{z}} - \hat{\mathbf{m}}\|^2 - \log(p_{\mathbf{y}}(\mathbf{y}|\mathbf{x})). \quad (6)$$

The PnP strategy consists of replacing the equation (4) by the application of a Gaussian denoiser  $\mathcal{D}_\sigma$ , corresponding to an implicit regularization:

$$\forall i \in \llbracket 1, d^2 \rrbracket, \quad \hat{\mathbf{z}}^i = \mathcal{D}_\sigma(\hat{\mathbf{x}}^i - \hat{\mathbf{m}}^i) \quad (7)$$

where  $\sigma = \frac{1}{\sqrt{\beta}}$  controls the filtering strength.

- 4) At the end of the ADMM algorithm, the  $d^2$  real-valued channels of  $\hat{\mathbf{x}}$  are recombined into an image of complex covariance matrices, and a matrix exponential is applied to obtain the final result  $\hat{\mathbf{\Sigma}}$ .

Like MIDAL, MuLoG assumes the independence of speckle from one pixel to the next and artifacts appear if speckle is spatially correlated. To suppress these artifacts, we propose in Sec.II-D to improve the robustness of the Gaussian denoiser to spatially correlated noise. Before discussing this robustification strategy, we present in the next paragraph the Gaussian denoiser we selected in this work.

### C. DRUNet: A versatile architecture for Plug-and-Play strategies

We have considered the DRUNet architecture recently introduced in [36]. The DRUNet architecture, shown in Figure 2, is based on three different network architectures. The main part takes advantage of two efficient architectures, the UNet [37], which is presented as a frugal architecture in terms of training dataset requirements, and the RESNet [38]. DRUNet consists of a contraction (downscaling) followed by a symmetric expansion (upscaling) and incorporates residual blocks between the scaling layers. The first layer increases the number of channels to 64, and is then doubled after each downsampling operation.

It is well-known that the noise level of the assumed Gaussian noise in PnP strategies can vary from one iteration to the next. Our choice was mainly motivated by the need for an architecture that can handle a wide range of noise levels with a single model. DRUNet verifies this condition by taking as input a noisy image with an additional channel defining the noise standard deviation, as initially proposed in the FFDNet architecture. In addition, DRUNet may achieve better results thanks to the use of stride convolutions for the contraction phase instead of max-pooling (followed by a non-strided

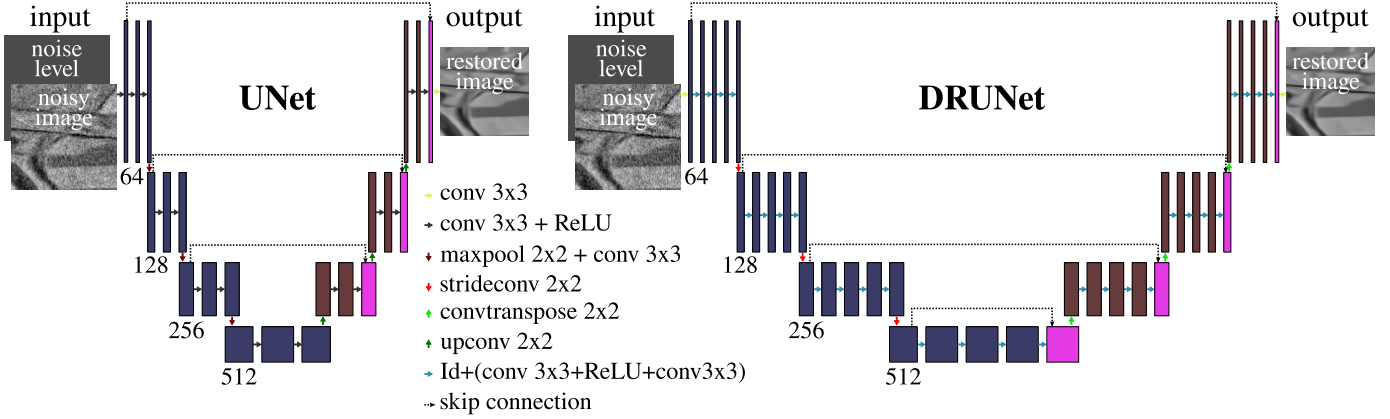


Figure 2: Comparison of UNet and DRUNet architectures.

convolution) [39] (see Figure 2). Stride convolutions apply the kernel to every element of the input whereas max-pooling applies it to a subset of the input. Thus, stride convolutions preserve more spatial information. This increases the receptive field of neurons in deeper layers of the network. As a result, the network can learn more complex features.

#### D. Generation of a training set with spatially-correlated Gaussian noise

The formation model of mono-channel SAR images illustrated in the figure 1 can be used to simulate spatially correlated speckle fields in accordance with the characteristics of a given radar sensor. Speckle is a multiplicative noise: in a fully developed speckle area, the complex amplitude of the scene can be written as the product of the scene’s amplitude  $\sqrt{r} \in \mathbb{R}_+^n$  with the complex speckle field  $s \in \mathbb{C}^n$ :  $\sqrt{r} \odot s$ , with  $\odot$  the element-wise product. The transfer function of the SAR imaging system introduces a spectral apodization that can be modeled as a 2D convolution product with the impulse response  $h$ , see for example [40]. The intensity  $|(\sqrt{r} \odot s) * h|^2$  of the resulting complex image is the quantity designated by the term “radar image” in the right part of the figure 1. As mentioned in section II-B, the logarithm (or matrix logarithm, in the case of polarimetric SAR images) is applied at the first step of the MuLoG algorithm. It has the effect of making the speckle approximately additive:  $y = \log |(\sqrt{r} \odot s) * h|^2 \approx x + \eta$  where  $x$  is the component describing the radar scene and  $\eta$  is the speckle component after the log transformation (this decomposition is exact for an ideal SAR response, i.e., when  $h$  corresponds to a Dirac distribution).

To adapt the Gaussian denoiser, we propose to train it to remove an additive noise component  $\eta \sim \mathcal{N}(0, C_\eta)$ , spatially correlated according to the covariance matrix  $C_\eta \in \mathbb{R}^{n \times n}$ , instead of a white Gaussian noise  $\eta \sim \mathcal{N}(0, \sigma^2 \text{Id})$

In the case of a homogeneous radar scene with a unitary reflectivity ( $r = 1$ ), the log-intensity image  $y = \log |s * h|^2 \approx \eta$  (the approximation stems from the discrepancy between Fisher-Tippett distribution followed by the log intensities in the absence of spatial correlations and the Gaussian distribution). In order to simulate Gaussian noises that are statistically as

close as possible to  $y$ , we set  $C_\eta = \text{Cov}[y]$  which we estimate from draws of  $y$  obtained from simulated complex speckle fields  $s$ . Since the speckle is spatially stationary (the radar imaging system is characterized by its transfer function), the covariance matrix  $C_\eta$  is itself stationary and can be characterized in the frequency domain by the power spectral density (PSD)  $\Psi_\eta$  ( $C_\eta$  is diagonalizable by the Fourier transform). We apply the periodogram method, consisting of averaging the power spectra of several random draws of  $\log |s * h|^2$  in order to estimate a spatial filter  $g$  capable of producing the expected spatial correlations:

$$g = \mathcal{F}^{-1}[\widehat{\Psi}_\eta^{1/2}], \text{ with } \widehat{\Psi}_\eta = \frac{1}{K} \sum_{k=1}^K |\mathcal{F}\{\log |s_k * h|^2\}|^2 \quad (8)$$

and where  $\mathcal{F}$  and  $\mathcal{F}^{-1}$  are the direct and inverse Fourier transforms. Thus, we can draw white noises  $\epsilon \sim \mathcal{N}(0, \text{I})$  and turn them into correlated noises  $\eta = g * \epsilon$  such that  $\text{Cov}[\eta] \approx \text{Cov}[y]$ .

The simulation process described above can also be used to generate noises for the training of a “generic” Gaussian denoiser that would be robust to spatial correlations associated to various sensors. To achieve this, one can replace  $\Psi_\eta$  in equation (8) with a random convex combination of PSDs linked to different covariance matrices. Figure 3 shows that such a generic denoiser leads to results that are comparable to those obtained with a denoiser trained specifically for the PSD of the sensor.

#### E. DRUNet training details

In this section, we detail the training process of DRUNet and show its superiority over the UNet architecture for our despeckling task through a visual comparison. The training is performed on noise-free Sentinel-1 images made publicly available by Dalsasso et al. [14]. Both networks are trained by minimizing the  $L_1$  loss using the ADAM optimizer with mini-batches of 16 patches of size  $128 \times 128$ . We divided our initial dataset into training and validation datasets, and we monitored the loss on the validation dataset and performed

<sup>1</sup>RADARSAT is an official brand of the Canadian Space Agency

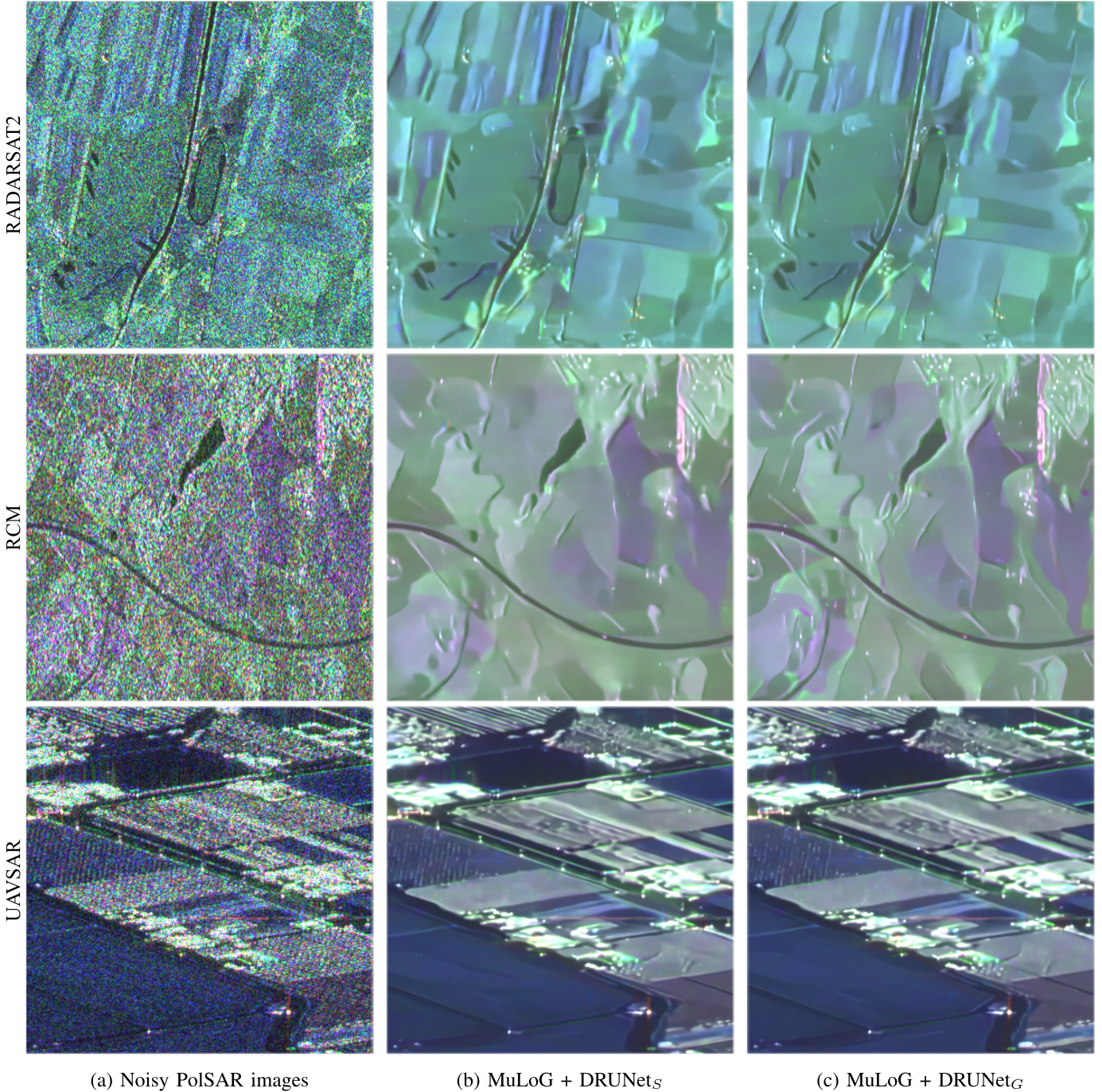
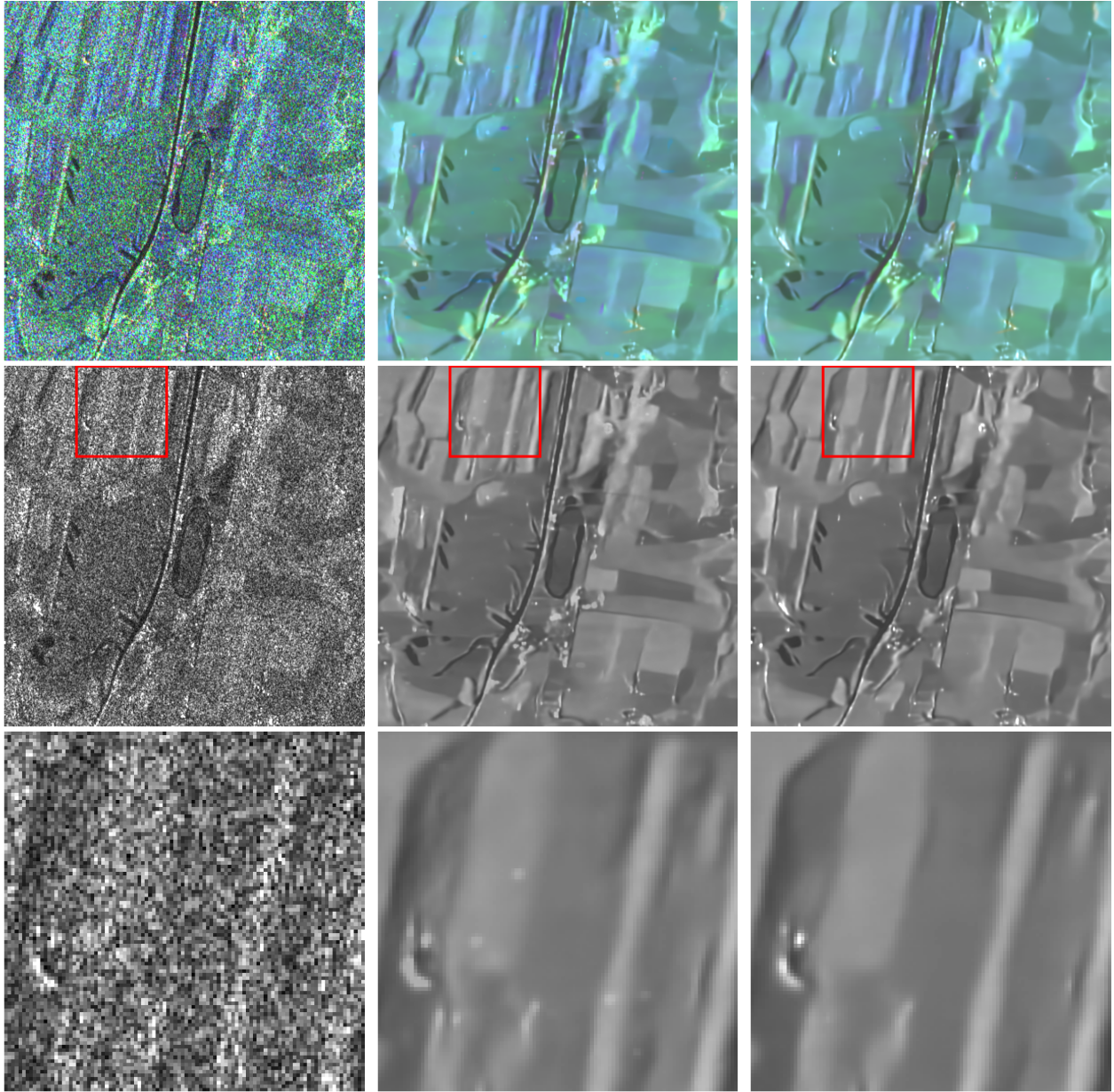


Figure 3: Visual comparison of MuLoG filtering results using DRUNet<sub>G</sub> trained on a unique spatial correlation and DRUNet<sub>G</sub> trained as a generic denoiser: from top to bottom are shown images acquired with RADARSAT-2, RCM <sup>1</sup>©Government of Canada (RADARSAT Constellation Mission) and UAVSAR ©NASA/JPL-Caltech sensors.

an early stopping to avoid overfitting. The training process for UNet and DRUNet takes about 30 minutes on Pytorch with an Nvidia Tesla A100 GPU. The results shown in figure 4 correspond to the case of RADARSAT-2 images and they indicate that DRUNet tends to produce sharper images than UNet.

### III. APPLICATION TO POLARIMETRIC SAR IMAGES

In this section, we compare our approach to existing methods on simulated and real SLC PolSAR images. The unavailability of network weights for deep-learning-based methods makes it difficult to compare with these methods. Therefore, the following methods are considered: the  $5 \times 5$  boxcar filter, the  $7 \times 7$  refined Lee filter [23], and the patch-based filter NL-SAR [31]. The source code of NL-SAR has been made publicly available by the authors of the paper and we used



(a) Initial RADARSAT-2 PolSAR image

(b) MuLoG + UNet

(c) MuLoG + DRUNet

Figure 4: Filtering results of a single-look RADARSAT-2 polarimetric image with MuLoG. First row: Pauli RGB representation of covariance matrix images, second row: intensity of the HH channel, last row: close up views of the area delineated by the red squares.

PolSARpro v6.0 implementation of refined Lee filter.

#### A. Performance assessment metrics

It has been stated that a good speckle filter method should have the following characteristics [41]:

- 1) strong speckle reduction in homogeneous areas;
- 2) scene feature preservation (texture, edges, . . . );
- 3) radiometric preservation;
- 4) absence of artifacts.

To evaluate our method we use the following criteria:

- Equivalent Number of Looks (ENL): it measures the degree of speckle removal in homogeneous areas and is defined as:

$$\text{ENL} = \frac{\mu_{\hat{I}_{\mathcal{H}}}^2}{\sigma_{\hat{I}_{\mathcal{H}}}^2}, \quad \hat{I}_{\mathcal{H}} = \{\hat{I}_{\rho}, \rho \in \mathcal{H}\} \quad (9)$$

where  $\mathcal{H}$  is the set of pixel indices defining a homogeneous area in image  $\hat{I}$ ,  $\mu_{\hat{I}_{\mathcal{H}}}^2$  and  $\sigma_{\hat{I}_{\mathcal{H}}}^2$  are the empirical mean and the empirical variance of  $\hat{I}_{\mathcal{Z}}$ , respectively. A higher value of the ENL indicates a stronger suppression of speckle.

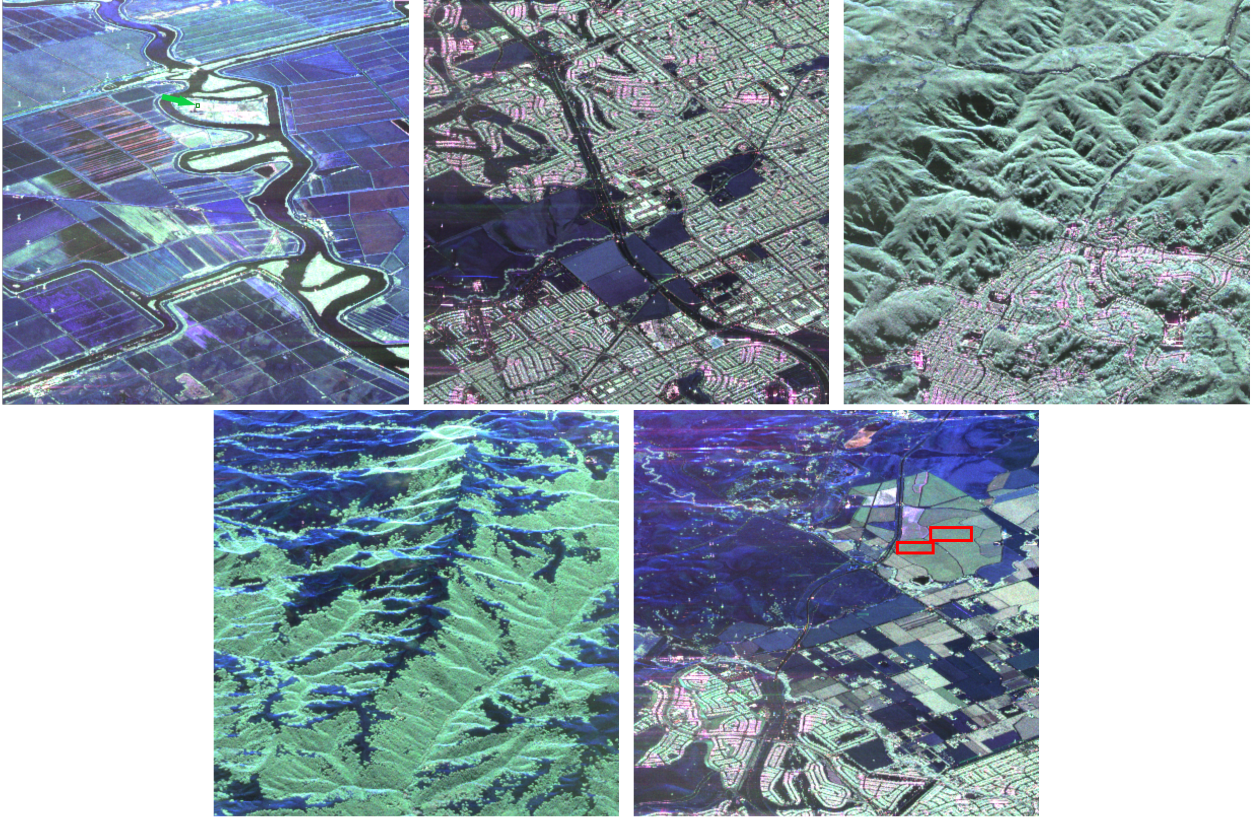


Figure 5: Ground truths computed from UAVSAR data ©NASA/JPL-Caltech. The colored boxes mark the regions where some of the metrics are computed: the green box indicated by the green arrow in the first image for co-pol and cross-pol, and the red boxes in the last image for ENL.

Metric	Boxcar	Refined Lee	NL-SAR	proposed	
				MuLoG+DRUNet <sub>S</sub>	MuLoG+DRUNet <sub>G</sub>
MSSIM $\uparrow^1$	0.814±0.0003	0.810±0.01	0.857±0.0005	<b>0.860±0.0007</b>	0.857±0.0009
GSIM $\downarrow_0$	0.169±0.0002	0.174±0.009	0.165±0.0004	<b>0.122±0.0002</b>	<b>0.123±0.0003</b>
ENL $\uparrow$	12.0	15.13	25.7	146.1	<b>291.8</b>

Table I: Quantitative evaluation of despeckling methods on images with simulated speckle (best performances are indicated in bold).

- Mean Structural Similarity Index Measure(MSSIM) [42]: this parameter is given by:

$$\text{MSSIM}(I, \hat{I}) = \frac{1}{n} \sum_{k=1}^n \text{SSIM}(I_k, \hat{I}_k) \quad (10)$$

with,

$$\text{SSIM}(I_k, \hat{I}_k) = \frac{(2\mu_{I_k} \mu_{\hat{I}_k} + \kappa_1)(2\sigma_{I_k \hat{I}_k} + \kappa_2)}{(\mu_{I_k}^2 + \mu_{\hat{I}_k}^2 + \kappa_1)(\sigma_{I_k}^2 + \sigma_{\hat{I}_k}^2 + \kappa_2)} \quad (11)$$

where  $n$  is the number of pixel of  $I$ ,  $\kappa_1$  and  $\kappa_2$  are constants and  $\mu_{I_k}$ ,  $\sigma_{I_k \hat{I}_k}$ , and  $\sigma_{I_k}^2$  are the empirical expectation, covariance, and variance, respectively, computed locally around pixel  $k$ . This criterion takes values between  $-1$  and  $1$  which are the worst and best values, respectively.

- Global SIMilarity (GSIM) [43]: the global similarity of two  $N$ -pixels multichannel SAR images  $\Sigma, \hat{\Sigma} \in \mathbb{C}^{n \times d \times d}$  is defined as

$$\text{GSIM}(\Sigma, \hat{\Sigma}) = \frac{1}{nd^2} \sum_{k=1}^n \|\log(\Sigma_k) - \log(\hat{\Sigma}_k)\|_F \quad (12)$$

where  $\|\cdot\|_F$  corresponds to the Frobenius norm and  $\log$  is the matrix logarithm. A lower value of this criterion indicates a higher degree of similarity.

- The Cloude-Pottier polarimetric decomposition parameters (entropy  $H$ , anisotropy  $A$ , and angle  $\alpha$ ) [44], [45]: they have been shown to be well-adapted for covariance matrix classification and thus can be used to indicate if covariance matrices within the same class are less scattered in the  $H$ - $A$ - $\alpha$  space thanks to the speckle filtering.
- The polarimetric signatures (co-pol and cross-pol) [45]–[47]: the polarimetric signature  $P \in \mathbb{R}^+$  of a target

represented by the covariance matrix  $\mathbf{C}_k \in \mathbb{C}^{d \times d}$  at a pixel  $k$  allows to visualize the response of the target under different settings (polarization of the waves, relative position of the target to the illumination source, ...). It is defined as follows:

$$\begin{aligned} \mathbf{P} &= \begin{pmatrix} 1 & \cos(2\phi_i)\cos(2\psi_i) & \cos(2\phi_i)\sin(2\psi_i) & \sin(2\phi_i) \\ \cos(2\phi_j)\cos(2\psi_j) & \cos(2\phi_j)\sin(2\psi_j) & \sin(2\phi_j) \end{pmatrix}^t \\ &\times \mathbf{K} \times \\ &\begin{pmatrix} 1 & \cos(2\phi_j)\cos(2\psi_j) & \cos(2\phi_j)\sin(2\psi_j) & \sin(2\phi_j) \end{pmatrix}^t \end{aligned} \quad (13)$$

where  $\mathbf{K}$  is the Kennaugh matrix [48] associated to  $\mathbf{C}_k$ , the pairs  $(\phi_i, \psi_i)$ , and  $(\phi_j, \psi_j)$  of orientation angle  $\psi \in [-\frac{\pi}{2}, \frac{\pi}{2}]$  and ellipticity angle  $\phi \in [-\frac{\pi}{4}, \frac{\pi}{4}]$  correspond respectively to the parameters describing the polarization state of the incident and backscattered waves. There is an infinity of possible signatures but the most used in despeckling quality assessment are the co-pol which corresponds to the case where the polarization is invariant in emission and reception i.e  $\phi_j = \phi_i$  and  $\psi_j = \psi_i$ , and the cross-pol which corresponds to the case where the polarization in emission and reception are orthogonal i.e  $\phi_j = -\phi_i$  and  $\psi_j = \psi_i + \frac{\pi}{2}$ .

The first two criteria of our list are defined for intensity images, we extend them to PolSAR images by averaging their values over the three intensity images corresponding to the diagonal values of the covariance matrices.

### B. Results on simulated data

The experiences in this section have been conducted considering the spatial correlation associated to RADARSAT-2 high-resolution images ( $12 \times 12$  meters). The ground truths were obtained by applying a  $7 \times 15$  multi-looking followed by downsampling to a UAVSAR noisy SLC PolSAR image with  $1.8 \times 0.8$  meters pixels (respectively in the range and azimuth directions). This multilooking produced almost speckle-free PolSAR images (an equivalent number of looks equal to 22 has been estimated on these images) with a spatial resolution close to RADARSAT-2 images, as can be seen in figure 5 representing five  $400 \times 400$  images with a variety of areas including water, fields, mountains, forests, and human constructions.

For each of the five images represented in figure 5, we simulated 10 independent speckled SLC versions with the following procedure. Starting from the ground truth PolSAR image of covariance matrices  $\Sigma \in \mathbb{C}^{n \times 3 \times 3}$ , we perform the pixel-wise Cholesky decomposition: at each pixel  $i$ , we find the unique lower triangular matrix with real positive diagonal elements matrix  $\mathbf{A}_i$  such that  $\Sigma_i = \mathbf{A}_i \mathbf{A}_i^*$ . Diffusion vectors  $\mathbf{k}_i \sim \mathcal{N}_c(\Sigma_i)$  distributed according to equation (1) can then be obtained by drawing standard circular Gaussian random vectors  $\epsilon \sim \mathcal{N}_c(\mathbf{I})$  and multiplying them with matrix  $\mathbf{A}_i$ :  $\mathbf{k}_i = \mathbf{A}_i \epsilon$ . The SAR transfer function can then be applied to each channel of the simulated complex-valued SLC images  $\mathbf{k}$ , according to the model discussed in Section II-D.

Table I shows the results of the quantitative comparison of the proposed method with the Boxcar filter, the Refined Lee filter, and NL-SAR on the simulated data using the first five

	Refined Lee			NL-SAR			proposed MuLoG+DRUNet <sub>G</sub>		
	①	②	③	①	②	③	①	②	③
ENL	7.04	7.71	8	9.19	26.53	14	<b>22.90</b>	<b>62.57</b>	<b>84</b>

Table II: Equivalent number of looks (ENL) reached by reference methods and the proposed polarimetric restoration technique on 3 high-resolution airborne PolSAR images: ① E-SAR image from the DLR, ② F-SAR image from the DLR, ③ SETHI image from the ONERA.

metrics of the above list. It represents the global mean of the obtained results and the mean of the corresponding standard deviations computed separately for each ground truth. As it can be seen our method outperforms the others (the results used for this analysis can be viewed in a pdf file shared with the code). The co-pol and cross-pol signatures shown in figure 6 also indicate that the proposed method restores polarimetric properties close to the reference signatures. Values of the ENL are large ( $>100$ ) with our method, which indicates a strong smoothing in the output images. Only the order of magnitude of the ENL should be compared since the sole maximization of the ENL is not recommended as it captures both positive effects (speckle suppression) and negative effects (over-smoothing and loss of texture/details).

### C. Results on real data

In this section, we present visual and quantitative results on three real mono-look polarimetric SAR images captured by different high-resolution remote sensing sensors: ESAR (DLR), FSAR (DLR), and SETHI (ONERA). The spatial dimensions of the images are  $512 \times 512$ ,  $1014 \times 1014$ , and  $1024 \times 1024$  pixels, respectively.

The despeckled images presented in figure 7 show that speckle fluctuations are reduced by all filtering techniques and that the proposed method performs a stronger smoothing of homogeneous areas while preserving geometrical details. Finally, in the figure 8 representing 3D scattergrams of the Cloude-Pottier polarimetric decomposition parameters for three distinct homogenous areas of the ESAR image, we can observe that, as expected from a despeckling method, the distribution of the parameters for the despeckled images 8(b-d) is much more clustered than for the speckled image 8(a). The clusters are even more separable with our method, indicating a performance compared to NL-SAR or the refined Lee filter.

We describe in the next section how our robust polarimetric despeckling algorithm MuLoG+DRUNet can also be included into a multi-temporal filtering framework.

## IV. EXTENSION TO MULTI-TEMPORAL POLARIMETRIC IMAGES: RABASAR-POLAR

Several constellations of satellites such as RCM, TerraSAR-X, Sentinel-1 give access to long time series of polarimetric images. The increasing availability of these time series has encouraged the development of methods that take advantage of the temporal redundancy to improve the speckle filtering.

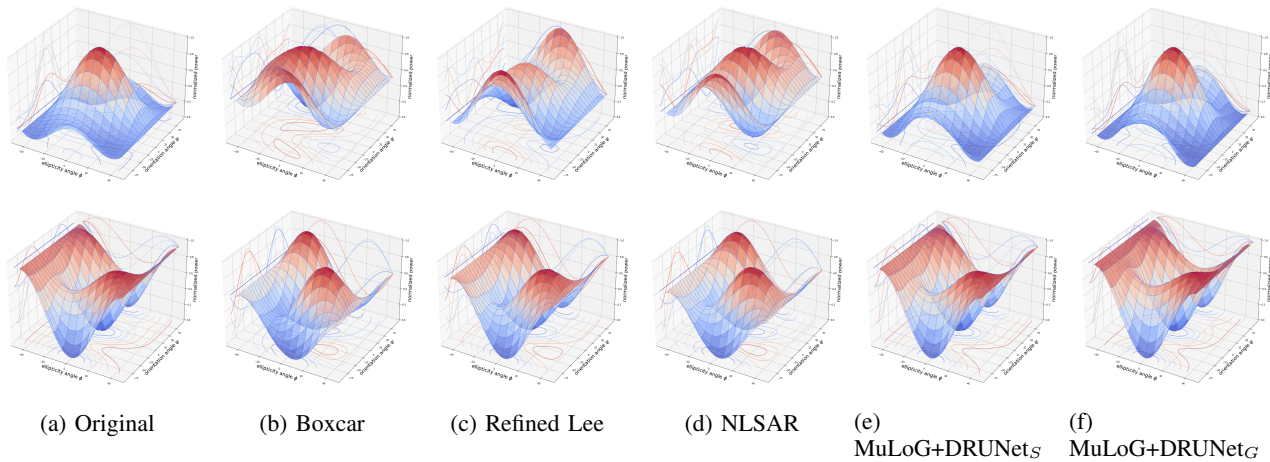


Figure 6: Co-pol (first row) and cross-pol (second) computed from the average covariance matrix of the  $3 \times 3$  area of the first image in figure 5 mark by a green box.

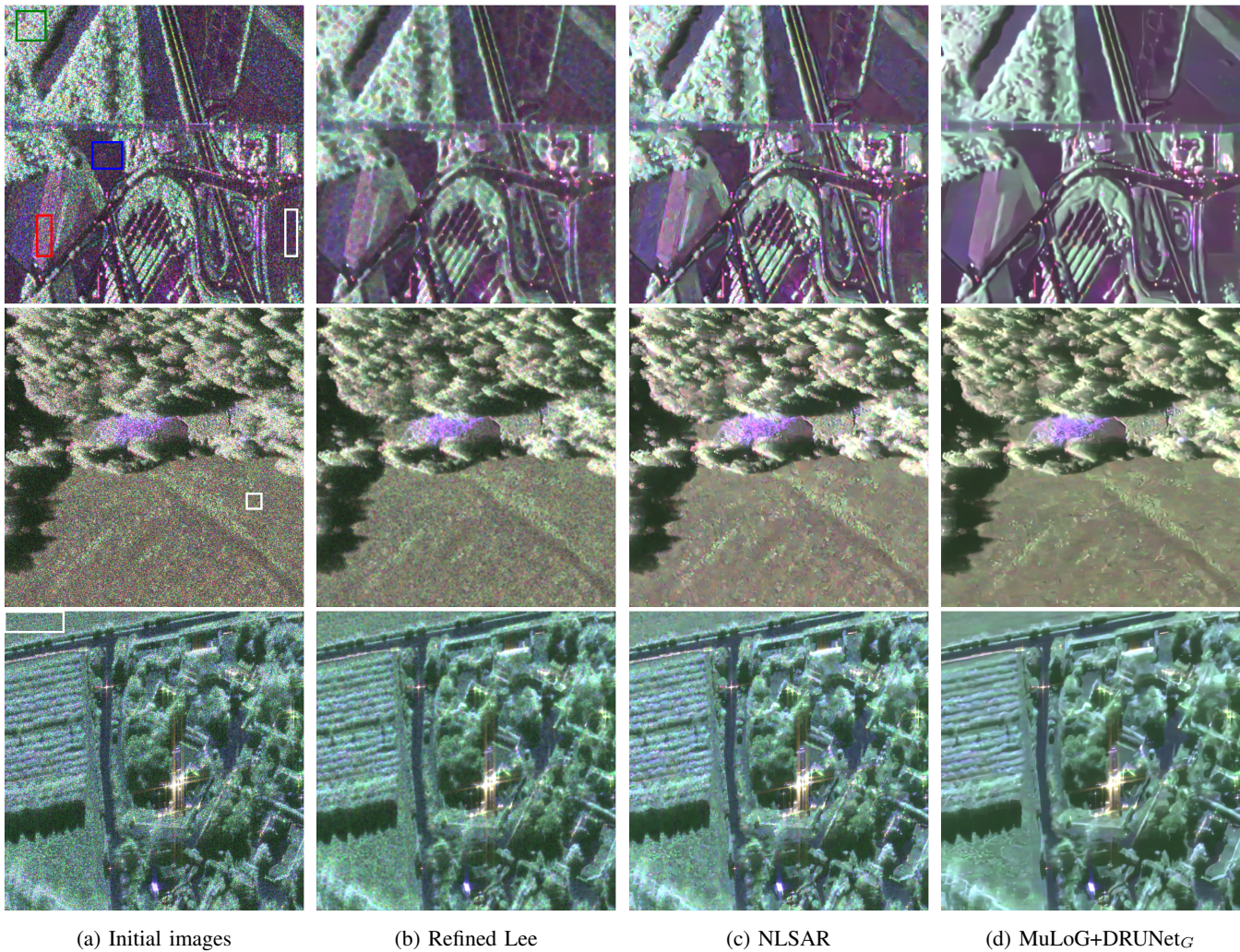


Figure 7: Filtering results of high-resolution PolSAR images acquired by E-SAR ©DLR, F-SAR ©DLR and SETHI ©ONERA sensors. The colored boxes in the left column images show the boundaries of the regions where the metrics are computed: white for ENL and the others for the Cloude-Pottier polarimetric decomposition.

In the following sections, we recall briefly the multi-temporal mono-channel SAR filter RABASAR [49] and present its

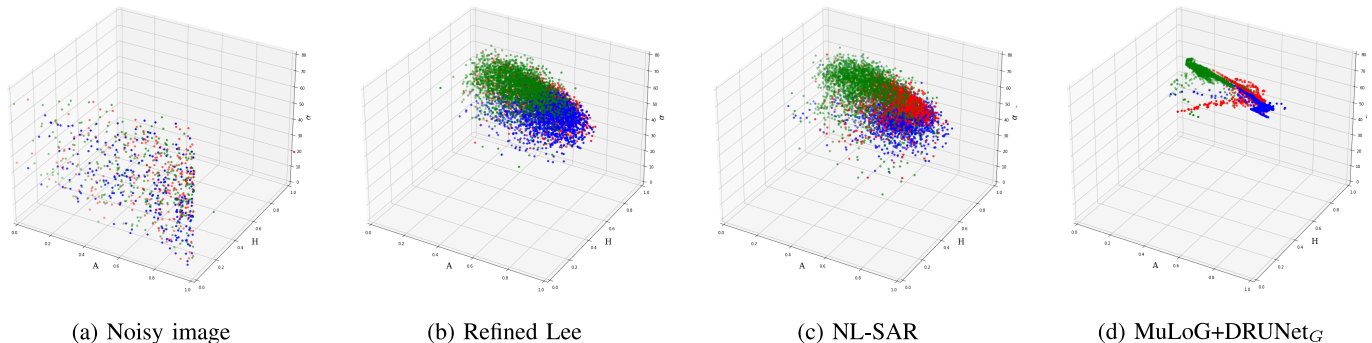


Figure 8: 3D scattergram of the Cloude-Pottier polarimetric decomposition parameters for the three homogeneous regions in the E-SAR image indicated by the red, green and blue boxes.

extension to polarimetric data.

#### A. Ratio-based filtering: RABASAR

The RABASAR method has been proposed to filter intensity SAR images. It exploits a time series of intensity SAR images of the same area to filter an image. It can be divided into the following three main steps, illustrated on Figure 9:

- The first step consists in summarizing the geometrical information in the time series into an image called the "super-image" due to its very low speckle level. This summary image is a first estimate of the reflectivity of the image to be filtered. The simplest way to compute the super-image is to take the mean of all the elements of the time series which is a good estimator when there are no strong changes in the scene over time. Other formulas to account for changes in the scene have been proposed and studied in [49], [50].
- The second step is to form a ratio image, by computing a pixel-by-pixel division of the noisy image to be filtered by the "super-image". The resulting image contains fewer structures than the original noisy image and is, therefore, easier to denoise because there is less risk of removing useful information. This ratio image can be filtered using the MuLoG algorithm.
- In the last step, the final estimation is obtained by re-multiplying the filtered ratio with the "super-image".

It has been shown in [49] that the RABASAR method leads to a good filtering level and better structure preservation than state-of-the-art multi-temporal denoising methods such as 2SPPB [51] and MSAR-BM3D [52]. The same level of performance is expected from its extension to polarimetric images. As usual, dealing with polarimetric data is more challenging. Indeed, the transition from the mono-channel case is not straightforward due to the special properties of covariance matrices. To generalize RABASAR to PolSAR images the definition of the ratio image needs to be adapted. Suitable definitions of the ratio between a polarimetric noisy image  $\mathbf{C}$  and the super-image  $\hat{\Sigma}^{\text{super}}$  are such that the ratio matrix  $\mathbf{R}_i$  at pixel  $i$  is distributed according to  $\mathcal{W}(\mathbf{I})$  when  $\mathbf{C}_i \sim \mathcal{W}(\hat{\Sigma}_i^{\text{super}})$ , i.e., it follows a white speckle noise in the absence of change with respect to the "super-image". Let

$\hat{\Sigma}_i^{\text{super}} = \mathbf{A}_i \mathbf{A}_i^*$  be a matrix factorization (this factorization is not unique). Then  $\mathbf{A}_i^{-1} \mathbf{C}_i \mathbf{A}_i^{*-1}$  is distributed according to  $\mathcal{W}(\mathbf{I})$  provided that  $\mathbf{C}_i \sim \mathcal{W}(\hat{\Sigma}_i^{\text{super}})$ .

*Proof.* Let  $\{\mathbf{k}_\ell\}_{\ell=1..L}$  be  $L$  random vectors independently and identically distributed according to a circular complex Gaussian distribution with unit covariance matrix  $\mathcal{N}_c(\mathbf{I})$ . The vectors  $\{\mathbf{A}_i \mathbf{k}_\ell\}_{\ell=1..L}$  then follow the distribution  $\mathcal{N}_c(\mathbf{A}_i \mathbf{A}_i^*)$ , i.e.,  $\mathcal{N}_c(\hat{\Sigma}_i^{\text{super}})$ . The empirical covariance  $\mathbf{C}_i = \frac{1}{L} \sum_{\ell=1}^L (\mathbf{A}_i \mathbf{k}_\ell)(\mathbf{A}_i \mathbf{k}_\ell)^*$  thus follows the Wishart distribution  $\mathcal{W}(\hat{\Sigma}_i^{\text{super}})$ . The corresponding ratio matrix  $\mathbf{R}_i \equiv \mathbf{A}_i^{-1} \mathbf{C}_i \mathbf{A}_i^{*-1} = \frac{1}{L} \sum_{\ell=1}^L \mathbf{A}_i^* (\mathbf{A}_i \mathbf{k}_\ell)(\mathbf{A}_i \mathbf{k}_\ell)^* \mathbf{A}_i^{-1} = \frac{1}{L} \sum_{\ell=1}^L \mathbf{k}_\ell \mathbf{k}_\ell^*$  then follows the Wishart distribution  $\mathcal{W}(\mathbf{I})$ .  $\square$

Satisfactory factorizations include the Cholesky factorization (where matrix  $\mathbf{A}_i$  is triangular with a positive diagonal) and the square root. The square root factorization has been used in all our experiments.

The proposed ratio-based polarimetric filtering is:

$$\hat{\mathbf{C}} = \mathbf{A} \mathcal{D}\{\mathbf{A}^{-1} \mathbf{C} \mathbf{A}^{*-1}\} \mathbf{A}^*, \quad (14)$$

where  $\mathcal{D}\{\}$  denotes the polarimetric despeckling operation, typically performed by MuLoG with our Gaussian denoiser robust to spatially-correlated speckle, and matrix products are applied at each pixel of the images ( $\mathbf{A} \in \mathbb{C}^{n \times d \times d}$ ,  $\mathbf{C} \in \mathbb{C}^{n \times d \times d}$ , and  $\hat{\mathbf{C}} \in \mathbb{C}^{n \times d \times d}$  are fields of matrices, only the despeckling operation  $\mathcal{D}\{\}$  is applied spatially, the other operations being performed pixelwise).

#### B. Experiments

In this section, we present the qualitative and quantitative results of RABASAR's extension to PolSAR images.

We considered a temporal stack of 17 PolSAR images that were acquired by the RADARSAT-2 sensor in a 9 months period. The performance of MuLoG embedded with the "generic" Gaussian denoiser is visually compared with the performance of RABASAR applied to the downsampled dataset, and RABASAR applied to the original dataset using MuLoG embedded with BMD3 and the "generic" denoiser, respectively. The results are shown in the figure 10. Although RABASAR allows to retrieve more structures, thanks to their

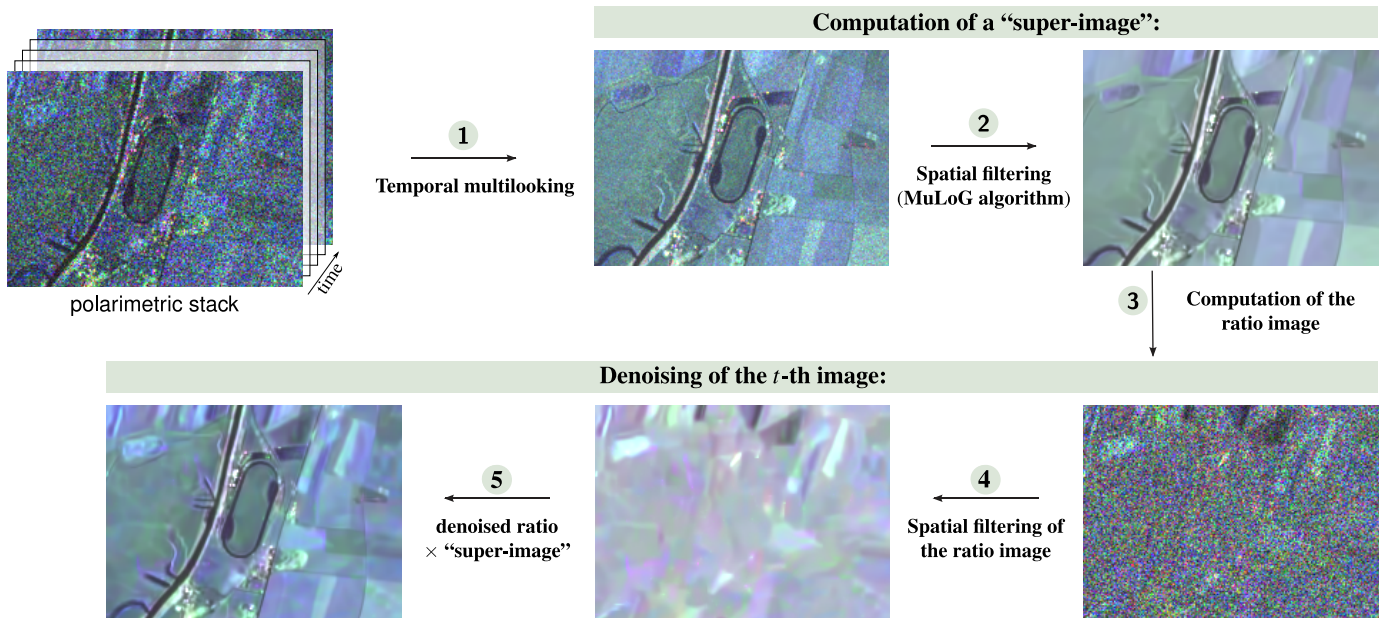


Figure 9: Scheme of the main steps of ratio-based filtering for polarimetric SAR images.

storage in the super-image (mostly temporally stable structures), the figure 10c illustrates the loss of information caused by the downsampling process. The use of our approach in the RABASAR method helps to obtain very detailed restorations 10d containing the structures specific to the image being denoised as well as the temporally stable structures which are not retrieved in the mono-date case 10b. To further illustrate the improvement in restoration quality offered by the RABASAR framework compared to the mono-date case, attention is directed towards a small area containing a fine structure barely visible in the noisy image in figure 11. Using a mask computed on the image restored with RABASAR, a ratio between the average intensity of the homogeneous area below the structure and the average intensity in the structure is computed on the HV-intensity images from the noisy PolSAR image, and the results obtained in mono-date and multi-temporal configurations. The results, indicated within the legend of the respective images in 11, show that the ratio is better preserved with RABASAR.

## V. CONCLUSION

Due to the difficulty of handling complex-valued covariance matrices, the literature on polarimetric SAR image despeckling is much less extended than for intensity SAR images. By performing a matrix-logarithm and decomposition into real-valued channels that can be denoised independently, MuLoG simplifies this problem. Yet, the statistical model of speckle used as starting point to derive the MuLoG algorithm ignores spatial correlations of speckle that are present in actual SAR images. In this paper, we proposed a solution to this problem that exploits the learning capabilities of deep-learning models in the PnP approach adopted in MuLoG. We proposed to train a deep-learning-based Gaussian denoiser to be robust to spatial correlations. We have shown that it is possible

to improve the robustness of our despeckling method to the spatial correlations of a range of sensors with a single neural network. Our approach leads to a versatile method for multi-channel SAR image despeckling. From a practical point of view, it simplifies the training problem of deep neural networks for PolSAR imagery which is reduced to mono-channel filtering (simplifying the constitution of the training set). The downside of this simplified single-channel processing step is the requirement to perform several iterations to produce a despeckled image ( $T \times d^2$  single-channel denoising operations for  $T$  steps of the ADMM loop on  $d$ -channel SAR images, see table III). Despeckling techniques based on a single pass in a feed-forward network can be typically  $T$  times faster, but are harder to train and can not readily handle SAR images with different number of channels, e.g. InSAR or PolInSAR. We hope that, by providing the code and network weights of our one-network-fits-all MuLoG approach, deep-learning-based polarimetric despeckling will be more routinely applied in a wide range of applications of SAR imaging.

## ACKNOWLEDGMENTS

This project has been partially funded by ASTRAL project (ANR-21-ASTR-0011) and by the grant n°R-S19/OT-0003-086 of the French space agency (CNES).

SETHI images were acquired by ONERA and processed in the framework of ALYS project (ANR-15-ASTR-0002). RADARSAT Constellation Mission images have been provided by the Canadian Space agency, and E-SAR and F-SAR aerial images have been provided by the German Space Agency (DLR).

## REFERENCES

- [1] J.-S. Lee and E. Pottier, *Polarimetric radar imaging: from basics to applications*. CRC press, 2017.

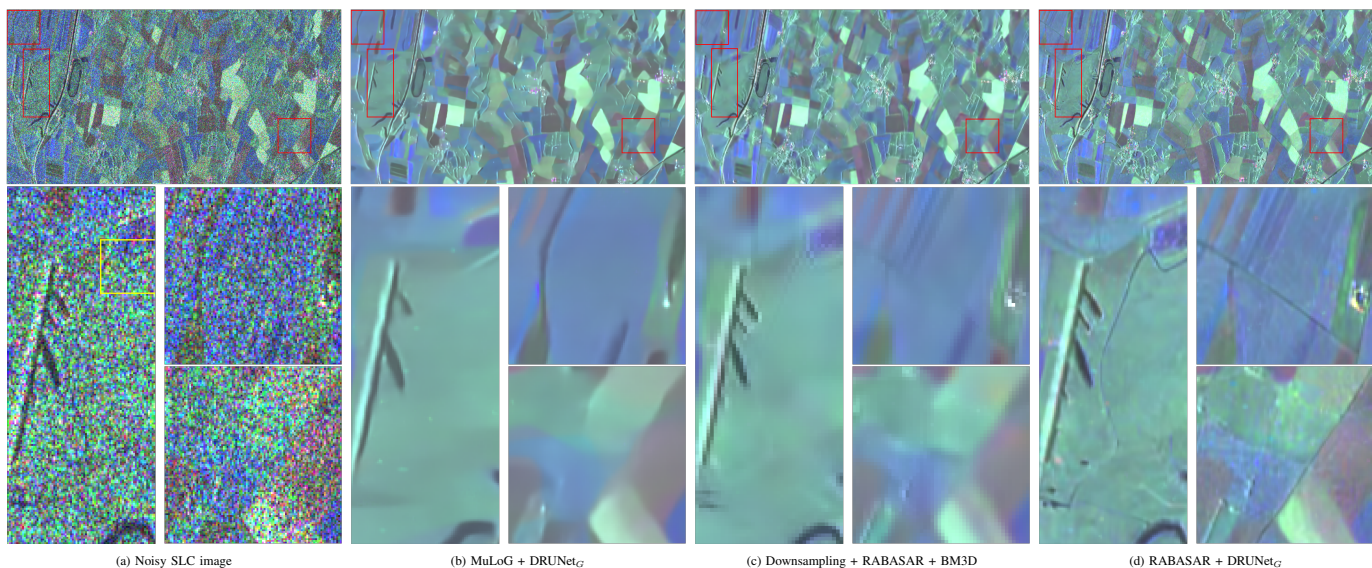


Figure 10: Performance comparison of mono-date and multitemporal despeckling approaches.

Image size	$d^2$	Gaussian denoiser	Time for GD	Time for FTP
512 × 512	1×1	BM3D	10.02s	0.42s
		DRUNet	1.32s	
1024 × 1024	1×1	BM3D	41.13s	3.03s
		DRUNet	4.62s	
512 × 512	3×3	BM3D	1min 33.88s	25.19s
		DRUNet	8.67s	
1024 × 1024	3×3	BM3D	6min 15s	2min 1.81s
		DRUNet	35.58s	

Table III: Computation time on an 'Intel(R) Core(TM) i5-9300H CPU @ 2.40GHz': Time for GD and Time for FTP correspond to the execution time of the Gaussian denoiser on the  $d^2$  channels and the estimation of the fidelity-term proximal operator, respectively; the second task is performed in parallel on different cores using the separability of the corresponding equation [27].

- [2] A. Moreira, P. Prats-Iraola, M. Younis, G. Krieger, I. Hajnsek, and K. P. Papathanassiou, "A tutorial on synthetic aperture radar," *IEEE Geoscience and remote sensing magazine*, vol. 1, no. 1, pp. 6–43, 2013.
- [3] J.-S. Lee, "Digital Image Enhancement and Noise Filtering by Use of Local Statistics," *IEEE Transactions on Pattern Analysis and Machine Intelligence*, vol. PAMI-2, no. 2, pp. 165–168, 1980.
- [4] Z. Shi and K. B. Fung, "A Comparison of Digital Speckle Filters," *Proceedings of IGARSS 94*, pp. 2129–2133.
- [5] C.-A. Deledalle, L. Denis, G. Poggi, F. Tupin, and L. Verdoliva, "Exploiting patch similarity for SAR image processing: The nonlocal paradigm," *IEEE Signal Processing Magazine*, vol. 31, no. 4, pp. 69–78, 2014.
- [6] G. Aubert and J.-F. Aujol, "A variational approach to removing multiplicative noise," *SIAM journal on applied mathematics*, vol. 68, no. 4, pp. 925–946, 2008.
- [7] J. M. Bioucas-Dias and M. A. T. Figueiredo, "Multiplicative Noise Removal Using Variable Splitting and Constrained Optimization," *IEEE Transactions on Image Processing*, vol. 19, pp. 1720–1730, 2009.
- [8] L. Denis, F. Tupin, J. Darbon, and M. Sigelle, "SAR image regularization with fast approximate discrete minimization," *IEEE Transactions on Image Processing*, vol. 18, no. 7, pp. 1588–1600, 2009.
- [9] G. Steidl and T. Teuber, "Removing multiplicative noise by Douglas-Rachford splitting methods," *Journal of Mathematical Imaging and Vision*, vol. 36, pp. 168–184, 2010.
- [10] G. Fracastoro, E. Magli, G. Poggi, G. Scarpa, D. Valsesia, and L. Verdoliva, "Deep learning methods for synthetic aperture radar image despeckling: An overview of trends and perspectives," *IEEE Geoscience and Remote Sensing Magazine*, vol. 9, no. 2, pp. 29–51, 2021.
- [11] B. Rasti, Y. Chang, E. Dalsasso, L. Denis, and P. Ghamisi, "Image restoration for remote sensing: Overview and toolbox," *IEEE Geoscience and Remote Sensing Magazine*, vol. 10, no. 2, pp. 201–230, 2021.
- [12] E. Dalsasso, L. Denis, M. Muzeau, and F. Tupin, "Self-supervised training strategies for SAR image despeckling with deep neural networks," in *EUSAR 2022; 14th European Conference on Synthetic Aperture Radar*. VDE, 2022, pp. 1–6.
- [13] G. Chierchia, D. Cozzolino, G. Poggi, and L. Verdoliva, "SAR image despeckling through convolutional neural networks," in *2017 IEEE International Geoscience and Remote Sensing Symposium (IGARSS)*. IEEE, 2017, pp. 5438–5441.
- [14] E. Dalsasso, X. Yang, L. Denis, F. Tupin, and W. Yang, "SAR image despeckling by deep neural networks: from a pre-trained model to an end-to-end training strategy," *Remote Sensing*, vol. 12, no. 16, p. 2636, 2020.
- [15] E. Dalsasso, L. Denis, and F. Tupin, "SAR2SAR: A Semi-Supervised Despeckling Algorithm for SAR Images," *IEEE Journal of Selected Topics in Applied Earth Observations and Remote Sensing*, vol. 14, pp. 4321–4329, 2020.
- [16] A. B. Molini, D. Valsesia, G. Fracastoro, and E. Magli, "Speckle2Void: Deep Self-Supervised SAR Despeckling With Blind-Spot Convolutional Neural Networks," *IEEE Transactions on Geoscience and Remote Sensing*, vol. 60, pp. 1–17, 2020.
- [17] E. Dalsasso, L. Denis, and F. Tupin, "As if by magic: self-supervised training of deep despeckling networks with MERLIN," *IEEE Transactions on Geoscience and Remote Sensing*, vol. 60, pp. 1–13, 2021.
- [18] S. Foucher, M. Beaulieu, F. Cavayas, and M. Dahmane, "Revisiting an iterative speckle filtering technique," in *IGARSS 2019 - 2019 IEEE International Geoscience and Remote Sensing Symposium*, 2019, pp. 5213–5216.
- [19] X. Yang, L. Denis, F. Tupin, and W. Yang, "Sar image despeckling using pre-trained convolutional neural network models," in *2019 Joint Urban Remote Sensing Event (JURSE)*. IEEE, 2019, pp. 1–4.
- [20] D. Tucker and L. C. Potter, "Polarimetric SAR Despeckling With

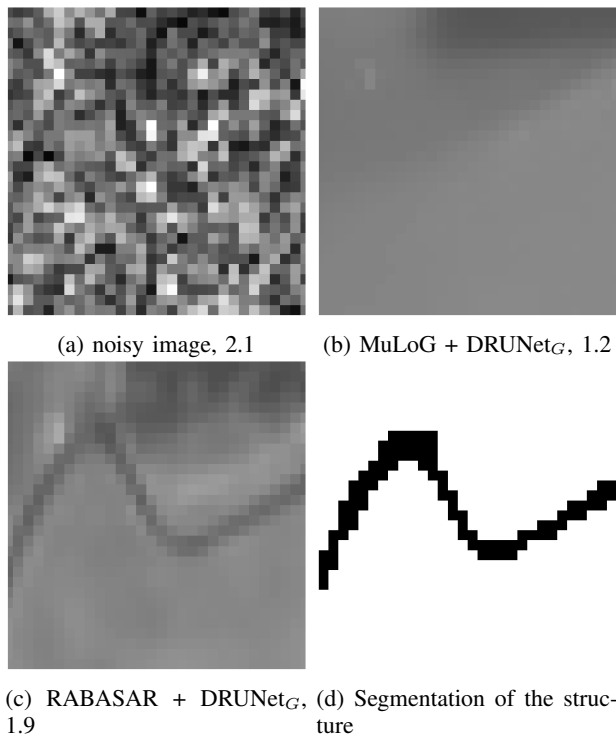


Figure 11: Zoom in on a  $30 \times 30$  area containing a fine structure delimited by the yellow box in the figure 10a: the HV-intensity images from the noisy PolSAR image, and the results obtained in mono-date and multi-temporal configurations are represented; the segmentation of the structure is performed on the image restored with RABASAR.

Convolutional Neural Networks,” *IEEE Transactions on Geoscience and Remote Sensing*, vol. 60, pp. 1–12, 2022.

- [21] A. G. Mullissa, C. Persello, and J. Reiche, “Despeckling Polarimetric SAR Data Using a Multistream Complex-Valued Fully Convolutional Network,” *IEEE Geoscience and Remote Sensing Letters*, vol. 19, pp. 1–5, 2022.
- [22] J.-S. Lee, “Digital image smoothing and the sigma filter,” *Computer vision, graphics, and image processing*, vol. 24, no. 2, pp. 255–269, 1983.
- [23] J.-S. Lee, M. Grunes, and G. de Grandi, “Polarimetric SAR speckle filtering and its implication for classification,” *IEEE Transactions on Geoscience and Remote Sensing*, vol. 37, no. 5, pp. 2363–2373, 1999.
- [24] D. Cozzolino, L. Verdoliva, G. Scarpa, and G. Poggi, “Nonlocal cnn sar image despeckling,” *Remote Sensing*, vol. 12, no. 6, p. 1006, 2020.
- [25] H. Lin, K. Jin, J. Yin, J. Yang, T. Zhang, F. Xu, and Y.-Q. Jin, “Residual in residual scaling networks for polarimetric sar image despeckling,” *IEEE Transactions on Geoscience and Remote Sensing*, 2023.
- [26] S. V. Venkatakrishnan, C. A. Bouman, and B. Wohlberg, “Plug-and-Play priors for model based reconstruction,” in *2013 IEEE Global Conference on Signal and Information Processing*, 2013, pp. 945–948.
- [27] C.-A. Deledalle, L. Denis, S. Tabti, and F. Tupin, “MuLoG, or How to Apply Gaussian Denoisers to Multi-Channel SAR Speckle Reduction?” *IEEE Transactions on Image Processing*, vol. 26, no. 9, pp. 4389–4403, 2017.
- [28] E. Dalsasso, L. Denis, and F. Tupin, “How to handle spatial correlations in SAR despeckling? Resampling strategies and deep learning approaches,” in *EUSAR 2021; 13th European Conference on Synthetic Aperture Radar*. VDE, 2021, pp. 1–6.
- [29] A. Lapini, T. Bianchi, F. Argenti, and L. Alparone, “Blind Speckle Decorrelation for SAR Image Despeckling,” *IEEE Transactions on Geoscience and Remote Sensing*, vol. 52, no. 2, pp. 1044–1058, 2014.
- [30] A. Arienzo, F. Argenti, L. Alparone, and M. Gherardelli, “Accurate Despeckling and Estimation of Polarimetric Features by Means of a Spatial Decorrelation of the Noise in Complex PolSAR Data,” *Remote Sensing*, vol. 12, no. 2, 2020. [Online]. Available: <https://www.mdpi.com/2072-4292/12/2/331>
- [31] C.-A. Deledalle, L. Denis, F. Tupin, A. Reigber, and M. Jäger, “NL-SAR: A Unified Nonlocal Framework for Resolution-Preserving (Pol)(In)SAR Denoising,” *IEEE Transactions on Geoscience and Remote Sensing*, vol. 53, no. 4, pp. 2021–2038, 2015.
- [32] C.-A. Deledalle, L. Denis, L. Ferro-Famil, J.-M. Nicolas, and F. Tupin, “Multi-Temporal Speckle Reduction of Polarimetric SAR Images: a Ratio-Based Approach,” in *IGARSS 2019 - 2019 IEEE International Geoscience and Remote Sensing Symposium*, 2019, pp. 899–902.
- [33] C.-A. Deledalle, L. Denis, and F. Tupin, “Speckle Reduction in Matrix-Log Domain for Synthetic Aperture Radar Imaging,” *Journal of Mathematical Imaging and Vision*, vol. 64, no. 3, p. 298–320, 2022.
- [34] J. W. Goodman, *Laser Speckle and Related Phenomena*. Springer Berlin, Heidelberg, 1984, ch. Statistical properties of laser speckle patterns, pp. 9–75.
- [35] N. R. Goodman, “Statistical Analysis Based on a Certain Multivariate Complex Gaussian Distribution (An Introduction),” *The Annals of Mathematical Statistics*, vol. 34, no. 1, pp. 152 – 177, 1963. [Online]. Available: <https://doi.org/10.1214/aoms/1177704250>
- [36] K. Zhang, Y. Li, W. Zuo, L. Zhang, L. Gool, and R. Timofte, “Plug-and-Play Image Restoration With Deep Denoiser Prior,” *IEEE Transactions on Pattern Analysis and Machine Intelligence*, vol. PP, pp. 1–1, 06 2021.
- [37] O. Ronneberger, P. Fischer, and T. Brox, “U-Net: Convolutional Networks for Biomedical Image Segmentation,” in *Medical Image Computing and Computer-Assisted Intervention – MICCAI 2015*, N. Navab, J. Hornegger, W. M. Wells, and A. F. Frangi, Eds. Cham: Springer International Publishing, 2015, pp. 234–241.
- [38] K. He, X. Zhang, S. Ren, and J. Sun, “Deep Residual Learning for Image Recognition,” *2016 IEEE Conference on Computer Vision and Pattern Recognition (CVPR)*, pp. 770–778, 2015.
- [39] J. T. Springenberg, A. Dosovitskiy, T. Brox, and M. A. Riedmiller, “Striving for Simplicity: The All Convolutional Net,” in *ICLR (workshop)*, vol. abs/1412.6806, 2014.
- [40] I. Meraoumia, E. Dalsasso, L. Denis, R. Abergel, and F. Tupin, “Multi-temporal speckle reduction with self-supervised deep neural networks,” *IEEE Transactions on Geoscience and Remote Sensing*, vol. 61, pp. 1–14, 2023.
- [41] G. Di Martino, M. Poderico, G. Poggi, D. Riccio, and L. Verdoliva, “Benchmarking Framework for SAR Despeckling,” *IEEE Transactions on Geoscience and Remote Sensing*, vol. 52, no. 3, pp. 1596–1615, 2014.
- [42] Z. Wang, A. Bovik, H. Sheikh, and E. Simoncelli, “Image quality assessment: from error visibility to structural similarity,” *IEEE Transactions on Image Processing*, vol. 13, no. 4, pp. 600–612, 2004.
- [43] J. Amao-Oliva, D. Torres-Román, I. Yanez-Vargas, A. Reigber, and M. Jäger, “The Beltrami SAR Framework for Multichannel Despeckling,” *IEEE Journal of Selected Topics in Applied Earth Observations and Remote Sensing*, vol. 12, no. 8, pp. 2989–3003, 2019.
- [44] S. Cloude and E. Pottier, “An entropy based classification scheme for land applications of polarimetric SAR,” *IEEE Transactions on Geoscience and Remote Sensing*, vol. 35, no. 1, pp. 68–78, 1997.
- [45] X. Ma, P. Wu, Y. Wu, and H. Shen, “A Review on Recent Developments in Fully Polarimetric SAR Image Despeckling,” *IEEE Journal of Selected Topics in Applied Earth Observations and Remote Sensing*, vol. 11, no. 3, pp. 743–758, 2018.
- [46] D. Tucker and L. C. Potter, “Polarimetric SAR Despeckling With Convolutional Neural Networks,” *IEEE Transactions on Geoscience and Remote Sensing*, vol. 60, pp. 1–12, 2022.
- [47] X. Nie, H. Qiao, and B. Zhang, “A Variational Model for PolSAR Data Speckle Reduction Based on the Wishart Distribution,” *IEEE Transactions on Image Processing*, vol. 24, no. 4, pp. 1209–1222, 2015.
- [48] B. You, J. Yang, J. Yin, and B. Xu, “Decomposition of the Kennaugh Matrix Based on a New Norm,” *IEEE Geoscience and Remote Sensing Letters*, vol. 11, 04 2014.
- [49] W. Zhao, C.-A. Deledalle, L. Denis, H. Maître, J.-M. Nicolas, and F. Tupin, “Ratio-Based Multitemporal SAR Images Denoising: RABASAR,” *IEEE Transactions on Geoscience and Remote Sensing*, vol. 57, no. 6, pp. 3552–3565, 2019.
- [50] N. Gasnier, L. Denis, and F. Tupin, “On the use and denoising of the temporal geometric mean for SAR time series,” *IEEE Geoscience and Remote Sensing Letters*, vol. 19, pp. 1–5, 2021.
- [51] X. Su, C.-A. Deledalle, F. Tupin, and H. Sun, “Two steps multi-temporal Non-Local Means for SAR images,” in *2012 IEEE International Geoscience and Remote Sensing Symposium*, 2012, pp. 2008–2011.
- [52] G. Chierchia, M. El Gheche, G. Scarpa, and L. Verdoliva, “Multitemporal SAR Image Despeckling Based on Block-Matching and Collaborative

Filtering." *IEEE Transactions on Geoscience and Remote Sensing*, vol. 55, no. 10, pp. 5467–5480, 2017.